RSC Advances

PAPER

View Article Online
View Journal | View Issue

Cite this: *RSC Adv.*, 2025, **15**, 34600

Tribological behavior of high-entropy alloy FeNiCrMn: a molecular dynamics simulation study

Nana Yang,*[a] Haorui Liu, *[ab] Furong Xu,[c] Qunli He,[a] Xin Liu[a] and Ning Mi[a]

Received 10th July 2025
Accepted 8th September 2025

DOI: 10.1039/d5ra04932f

rsc.li/rsc-advances

Co-free FeNiCrMn HEAs, as derivatives of the Cantor alloy, have attracted significant interest for their outstanding mechanical properties and cost-effectiveness. Exploring the fundamental mechanisms can facilitate the realization of improved composition design and enhanced modification of FeNiCrMn HEAs. Therefore, molecular dynamics simulations were employed to investigate the tribological behavior of the equiatomic FeNiCrMn high-entropy alloy, focusing on the effects of crystallographic orientation, sliding velocity, and indentation depth. The results reveal that the coefficient of friction (COF) remains relatively consistent across different crystallographic orientations, while the [1$\bar{1}$2] orientation exhibits lower dislocation density and more uniform atomic pile-up. Sliding velocity has a negligible impact on the COF, but higher velocities increase tangential forces due to strain-rate hardening. In contrast, deeper friction depths significantly elevate COF and subsurface damage, driven by enhanced dislocation nucleation and stress concentration. These results provide atomic-scale insights into the tribological mechanisms of FeNiCrMn HEA, offering guidance for its design in tribological environments.

1. Introduction

High-entropy alloys (HEAs), characterized by their multi-principal element compositions, exhibit four core effects: high-entropy effect, severe lattice distortion effect, cocktail effect, and sluggish diffusion effect.[1,2] These effects collectively endow HEAs with superior mechanical properties, including high strength, excellent corrosion resistance, and enhanced fatigue performance.[3,4] Due to the high hardness of HEAs with numerous strengthening mechanisms, HEAs hold potential for tribological applications in harsh environments, such as aerospace bearings, nuclear reactor components, and cryogenic machinery.

Wear constitutes a critical factor leading to the failure of mechanical equipment and components.[5] Hence, implementing effective control or reduction of material surface wear is crucial, which in turn contributes to energy conservation and cost reduction.[6] Numerous studies have investigated the tribological performance of different HEAs. Among these alloys, FeCoNiCrMn HEA, known as a Cantor alloy, is one of the most initially proposed and extensively researched HEA systems.[7] Li *et al.*[8] employed atomistic simulations to investigate the mechanical behavior of AlCrFeCuNi high-entropy alloys under uniaxial tensile loading. The results showed that the calculated elastic properties and stress–strain responses are in excellent agreement with recent experimental findings. Most importantly, the $AlCrFeCuNi_{1.4}$ HEA exhibits not only high strength but also good plasticity, consistent with experimental observations. Zhang *et al.*[9] employed molecular dynamics simulations combined with a physical model to investigate the effect of scratch depth on the microstructure and tribological properties of $FeCoCrNiAl_{0.5}$ HEAs. The results revealed that the scratching force increases significantly with increasing scratch depth. In the lower region of the scratch zone, pronounced atomic movements were observed, where the load applied in the normal direction drives atoms downward. Zhang *et al.*[10] demonstrated that CoCrFeNiMn high-entropy alloy exhibits better tribological properties than 304 stainless steel when sliding against Si_3N_4, as evidenced by lower wear rates of both the disk and its counterpart. Guo *et al.*[11] reported that Cr_3C_2-reinforced CoCrFeNiMn composites exhibit temperature-dependent tribological enhancement, where 10% Cr_3C_2 addition composite exhibited the optimal comprehensive mechanical and tribological properties. Zhang *et al.*[12] achieved WC-reinforced CoCrFeNiMn showing progressive wear rate reduction with increasing WC content, attributed to enhanced particle–matrix bonding and the transition from abrasive to stable wear behavior. While incorporating additional elements or hard reinforcements into FeCoNiCrMn alloys can improve the wear resistance and reduce coefficient of friction, the expensive nature of cobalt restricts widespread utilization of this system.[13,14] Consequently, the Co-free FeNiCrMn-based HEA, a derivative of the Cantor alloy, has attracted significant interest for its outstanding mechanical properties and cost-effectiveness. Yang *et al.*[15] demonstrated that boronized FeMnCrNi high-entropy

[a]School of Materials Engineering, Longdong University, Qingyang, 745000, China. E-mail: nanayang_material@163.com; lhr_tju@163.com
[b]School of Materials Science and Engineering, Lanzhou University of Technology, Lanzhou, 730050, China
[c]School of Mechanical Engineering, Lanzhou Petrochemical University of Vocational Technology, Lanzhou, 730060, China

alloys exhibit lower friction coefficients and wear rates compared to non-boronized counterparts across 20–600. Lu *et al.*[16] developed a Co-free CrFeNiNbx eutectic alloy with enhanced compressive strain compared to Co-containing variants, and compared with the Co-bearing eutectic, there was no obvious change in the morphology of the Co-free eutectic. Yang *et al.*[17] demonstrated that $Fe_{40}Mn_{20}Cr_{20}Ni_{20}$ HEA exhibits 20–30 times lower wear rates when sliding against Si_3N_4 compared to WC/Co or GCr15 counterfaces, suggesting that ceramic pairing should be prioritized for HEA moving components. Based on the above research findings, FeNiCrMn high-entropy alloys exhibit excellent mechanical properties; however, the underlying microscopic mechanisms supporting their application in tribological studies have not yet been fully established.

Compared with experimental approaches, molecular dynamics (MD) simulations are more time-efficient and cost-effective, while offering powerful capabilities for probing the microstructure and mechanical properties of materials at the atomic scale. Exploring the mechanisms through MD simulations can facilitate the realization of improved composition design and enhanced modification of HEAs. Zhou *et al.*[18] systematically investigated the effects of pressed depth, alloy composition, and sliding distance on the nanotribological behavior of Cu–Ni alloys, analyzing surface morphology evolution, frictional forces, dislocation density variations, and von Mises stress distributions to reveal atomic-scale deformation mechanisms. Li *et al.*[19] revealed the evolution process of phase structure and atomic-scale deformation mechanism of the NiAlCo alloy under high temperature and friction conditions by studying the effects of temperature, tip radius, sliding depth, and sliding distance on friction characteristics.

In this study, molecular dynamics simulations are employed to systematically investigate the tribological behavior of the FeNiCrMn high-entropy alloy, focusing on three critical parameters: crystallographic orientation, sliding velocity, and friction depth. A molecular dynamics model was developed for the FeNiCrMn HEA system, and the tangential force, normal force, and dislocation evolution were analyzed as functions of these variables. The fundamental mechanisms governing friction and wear are elucidated through atomic-scale analysis of lattice deformation, dislocation dynamics and stress propagation. Furthermore, the formation and interaction of key dislocation structures are investigated in detail to reveal the underlying deformation mechanisms. This work provides new insights into the nanotribological behavior of FeNiCrMn HEA and establishes a theoretical foundation for optimizing their wear resistance in engineering applications.

2. Computational methods and model construction

MD simulations were performed using the Large-scale Atomic/Molecular Massively Parallel Simulator (LAMMPS).[20] The first step involved determining the lattice constant of the equiatomic FeNiCrMn HEA. Taking Fe as the base element with a lattice constant of 3.61 Å, an initial bulk model with dimensions of 18 Å × 18 Å × 18 Å and an FCC crystal structure was constructed. Subsequently, the remaining elements (Ni, Cr, and Mn) were randomly substituted into the lattice to form a solid solution. Following equilibration, the finally measured lattice constant was 3.64 Å. Based on the optimized lattice constant, a new simulation model was constructed with crystallographic orientations of *X*-[1$\bar{1}$2], *Y*-[110] and *Z*-[$\bar{1}$11], and with dimensions of 101.9 Å × 200.2 Å × 149.2 Å, containing a total of 254 880 atoms. It is worth noting that in the FCC structure, the [110] direction is orthogonal to the (111) plane with the same Miller indices.

Thereafter, a spherical diamond abrasive tool with a radius of 15 Å was placed above the alloy surface. To eliminate boundary effects, periodic boundary conditions were applied along the *X* and *Y* directions, while a free boundary condition was used along the *Z* direction. The complete model configuration is illustrated in Fig. 1.

In this study, three types of atomic interactions are considered to comprehensively characterize the interfacial behavior within the simulation system. Specifically, the interactions among Fe, Ni, Cr, and Mn atoms in the model are described using the Embedded Atom Method (EAM) potential.[21,22] The total energy is calculated according to eqn (1):

$$E_i = \sum_i F_\alpha(\rho_i) + \frac{1}{2}\sum_{j\neq i}\varphi_{\alpha\beta}(r_{ij})$$
$$\rho_i = \sum_{j\neq i}\rho_\beta(r_{ij}) \quad (1)$$

where E_i is the total energy of atom i, $F_\alpha(\rho_i)$ denotes the embedding energy, which is a function of the local electron density ρ_i, $\varphi_{\alpha\beta}(r_{ij})$ represents the pairwise interaction between atoms i and j, with α and β denoting the chemical species of atoms i and j, respectively. r_{ij} is the interatomic distance between atoms i and j, ρ_β is the contribution to the electron charge density from atom j of type β at the location of atom i. For the diamond abrasive particle, the interactions between C–C atoms are described using the Tersoff potential.[23] However, since the abrasive tool is treated as a rigid body in the simulation, this potential is applied only during the model construction phase; consequently, the C–C interactions are not considered in the subsequent simulation process. Meanwhile, the interactions between Fe–C, Ni–C, Cr–C, and Mn–C atom pairs are described using the Lennard–Jones (L–J) potential. The

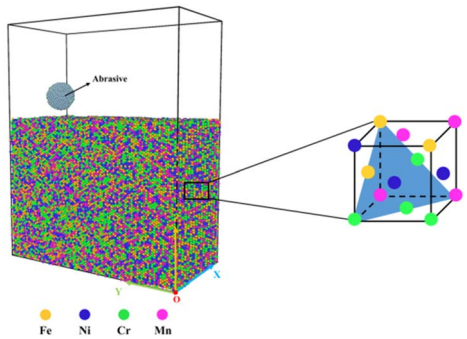

Fig. 1 Model of the FeNiCrMn high-entropy alloy.

Table 1 L–J potential parameters for atomic interactions in the system

Atom pair	ε (eV)	σ (Å)
Fe–C	0.0490	2.9897
Ni–C	0.0486	2.9645
Cr–C	0.0478	2.9993
Mn–C	0.0016	3.3768

specific L–J potential parameters used in the system are listed in Table 1.

After the model was constructed, the conjugate gradient algorithm was first employed to minimize the system energy and eliminate any unrealistic atomic configurations. Subsequently, the Nose–Hoover thermostat within the *NVT* ensemble was applied to equilibrate the system and set the initial temperature of the alloy to 300 K. Seven atomic layers at the bottom of the alloy were designated as a fixed boundary region to prevent translational motion of the entire model. The equilibration process was carried out in four sequential steps with a time step of 1 fs. In the first step, the temperature of the alloy model was ramped from 300 K to 1000 K over a period of 200 ps. In the second step, the model was maintained at 1000 K for 100 ps. In the third step, the system was cooled from 1000 K back to 300 K over 200 ps. Finally, in the fourth step, the temperature was held constant at 300 K for an additional 100 ps. Upon completion of these four steps, the model reached a thermodynamic equilibrium state, yielding an optimized atomic configuration for the given alloy composition.

The simulation of the alloy's friction and wear performance was conducted in two stages. First, the tribological behavior under different crystallographic orientations was investigated. The orientations of the three models are as follows: (1) *X*-[1$\bar{1}$2], *Y*-[110], *Z*-[$\bar{1}$11]; (2) *X*-[110], *Y*-[$\bar{1}$11], *Z*-[1$\bar{1}$2]; (3) *X*-[1$\bar{1}$2], *Y*-[110], *Z*-[$\bar{1}$11]. In all three models, the normal direction is aligned with the *Z*-axis, while the wear direction corresponds to the *Y*-axis.

Subsequently, one selected orientation was used to study the effects of varying friction depths and sliding velocities. During the friction process, the abrasive tool initially approached the alloy surface at a velocity of 15 Å ps^{-1} to establish rapid contact, followed by penetration into the alloy at a rate of 1 Å ps^{-1} until the target friction depth was reached. During this loading phase, the alloy system was controlled using the *NVT* ensemble. Subsequently, sliding was performed along the *Y*-axis at a predetermined velocity, with the system temperature maintained at 300 K. Throughout the sliding phase, all atoms except those in the fixed boundary layer were regulated by the *NVT* ensemble. The simulation results were analyzed and visualized using the OVITO software package.[24] The specific parameters of the model and simulation procedures are summarized in Table 2.

Table 2 Specific parameters of the model and simulation procedure

Parameters	Value
Potential function	EAM/L–J
Model dimensions	101.9 Å × 200.2 Å × 149.2 Å
Alloy elements	Fe; Ni; Cr; Mn
Abrasive tool radius	15 Å
Crystallographic orientation	[1$\bar{1}$2]; [110]; [$\bar{1}$11]
Temperature	300 K
Time step	1 fs
Friction velocity (V)	0.5 Å ps^{-1}; 1 Å ps^{-1}; 1.5 Å ps^{-1}
Friction depth (D)	10 Å; 15 Å; 20 Å
Number of atoms	254 880

3. Results and discussion

3.1 Effect of crystallographic orientation on tribological performance

To investigate the effect of crystallographic orientation on tribological performance, three models were constructed, with each subjected to sliding along the *Y*-axis. The surface in contact with the abrasive tool was oriented perpendicular to the *Z*-axis; therefore, the *Z*-axis orientation was designated as the variable for investigation. Three crystallographic orientations, namely [1$\bar{1}$2], [110], and [$\bar{1}$11], were selected for modeling. The sliding velocity was set to 1 Å ps^{-1}, the friction depth to 10 Å, and the sliding distance to 100 Å. To facilitate visualization, alloy atoms were color-coded along the *Z*-direction: atoms near the top surface of the model were colored red, and the color gradually transitioned to blue with decreasing height. Fig. 2 illustrates the surface morphology evolution of the three models during the friction process.

As sliding progresses, the abrasive tool disrupts the crystalline structure of the alloy, displacing atoms from their original lattice positions and causing atomic pile-up on the alloy surface. Under identical friction conditions, the models with different crystallographic orientations exhibit markedly distinct surface morphologies. For the [110] orientation as shown in Fig. 2(a), atomic accumulation is primarily concentrated in front of the abrasive particle, with a small amount also observed on both sides of the wear track. Overall, the pile-up area is relatively limited, and the atomic height distribution along the center of the wear track is uneven. In contrast, as shown in Fig. 2(b), for the [$\bar{1}$11] orientation, atoms accumulate both in front of the abrasive tool and along the sides of the wear track,

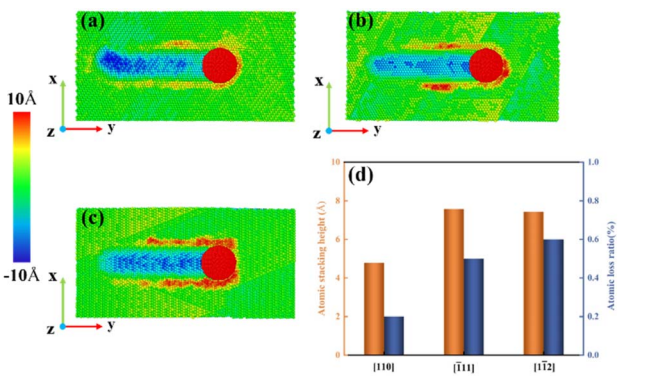

Fig. 2 Surface morphology of the alloy. (a) [110] orientation, (b) [$\bar{1}$11] orientation, (c) [1$\bar{1}$2] orientation, (d) maximum atomic pile-up height and atom loss ratio.

and the atomic distribution within the center of the wear track appears uniform. In Fig. 2(c), corresponding to the [1$\bar{1}$2] orientation, atoms predominantly accumulate symmetrically along both sides of the wear track, with no pile-up observed in front of the abrasive particle. The atomic distribution in the center of the wear track is uniform, and the accumulation on both sides is continuous without any observable discontinuities. This behavior indicates enhanced ductility in the [1$\bar{1}$2]-oriented model.[25] Fig. 2(d) presents a statistical comparison of the maximum atomic pile-up height and atom loss ratio for the three models during friction. The atom loss ratio is defined as the ratio of atoms in the surface pile-up region to the total number of atoms in the system. Overall, the [1$\bar{1}$2] orientation exhibits the highest atom loss ratio and a relatively large atomic pile-up height, suggesting more pronounced surface deformation under the same loading conditions.

During the frictional interaction between the abrasive tool and the top surface of the alloy, the generated forces induce subsurface damage within the alloy. Subsurface damage is a critical indicator of surface integrity, and its severity can be quantitatively characterized by the dislocation density derived from molecular dynamics simulations. Dislocation density is defined as the total length of dislocation lines per unit volume of the alloy. Given that the model volume remains constant throughout this study, the variation in dislocation density can be directly represented by the total dislocation line length. The dislocation lengths were calculated using the Dislocation Extraction Analysis (DXA) module in the OVITO software, and the statistical results are presented in Fig. 3.

During surface friction, the abrasive tool exerts force on the alloy, initiating a series of deformation processes. Prior to sliding, the particle indents into the alloy, breaking metallic bonds between constituent atoms and displacing them from their original lattice positions. This leads to local lattice distortion and defect formation around the abrasive. Once sliding begins, atoms in front of the abrasive tool are subjected to shear and compressive stresses. As the particle moves forward, these atoms are pushed out along the alloy surface, while frictional heating further contributes to the destruction of the local crystalline structure. The passage of the abrasive tool leaves behind a wear track, resulting in dislocation nucleation and the formation of subsurface damage. Fig. 3(a)–(c) show the instantaneous dislocation distributions for the three crystallographic orientations after a sliding distance of 100 Å. The results reveal significant differences in dislocation distribution among the orientations. In the [110] orientation, dislocations are primarily concentrated at the front of the abrasive tool and within the alloy interior. For the [$\bar{1}$11] orientation, dislocations are distributed near the abrasive front, beneath the wear track, and even at the bottom of the alloy. In the [1$\bar{1}$2] orientation, dislocations are mainly concentrated beneath the wear track and within the bulk of the alloy. These differences are attributed to the variation in activated slip systems due to differing crystallographic orientations, which determine how atomic planes respond to shear forces exerted by the abrasive. As shown in Fig. 3(d), the total dislocation line length increases with sliding distance. This trend reflects the progressive destruction of crystal planes by the abrasive particle, resulting in the generation of more defects and an increased number of dislocation nucleation sites, thereby elevating dislocation density. Overall, Shockley partial dislocations (with Burger vector $b = 1/6\langle 112\rangle$) dominate across all three orientations. Given that the (111) plane is the close-packed plane in FCC structures, dislocation nucleation and slip preferentially occur along this plane, leading to higher dislocation line lengths and more severe subsurface damage in the alloy.

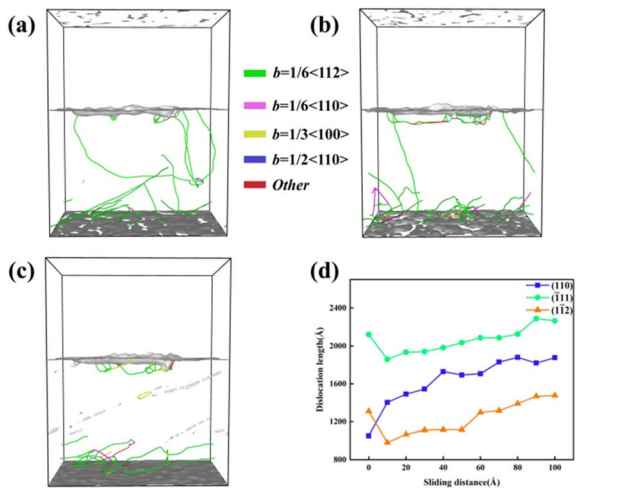

Fig. 3 Dislocation distribution and the variation of dislocation line length with sliding distance for the three crystallographic orientations. (a) [110] orientation, (b) [$\bar{1}$11] orientation, (c) [1$\bar{1}$2] orientation, (d) dislocation line length as a function of sliding distance.

The force exerted by the abrasive tool directly reflects the interfacial friction response, where the coefficient of friction (COF) serves as a primary evaluation metric. Generally, a lower COF correlates with reduced energy dissipation during sliding, thereby indicating superior frictional behavior.[26] Since the COF is intrinsically linked to both the tangential and normal forces acting on the abrasive particle, analyzing these forces and the resulting COF is essential for evaluating the friction and wear properties of materials. In this study, the tangential and normal forces acting on the abrasive tool during the steady-state sliding phase were averaged, and the standard deviation of the selected data points was used as the error bar in the plotted results. The steady-state friction phase is defined as the portion of the simulation in which the sliding distance exceeds the radius of the abrasive particle.

Fig. 4 presents the average tangential and normal forces experienced by the abrasive particle, as well as the COFs for the three crystallographic orientation models. As shown in Fig. 4(a), the average tangential and normal forces during sliding exhibit minimal variation across the different orientations. However, it is noteworthy that the [110] orientation exhibits relatively larger error bars in both tangential and normal forces, indicating pronounced stress fluctuations during the friction process. This observation is consistent with the non-uniform atomic height distribution observed in the wear track center of Fig. 2(a). Fig. 4(b) summarizes the COFs of the three models under

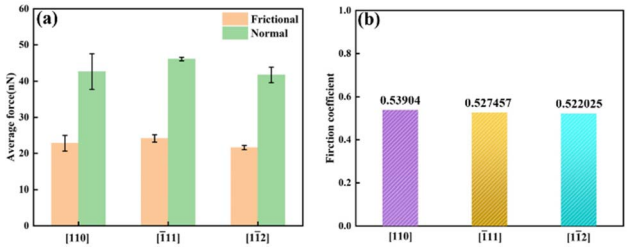

Fig. 4 Average forces and coefficient of friction during the sliding process for different crystallographic orientations. (a) Average tangential and normal forces for models with different orientations, (b) coefficient of friction for models with different orientations.

identical conditions. Overall, the COFs are nearly identical across all orientations, suggesting that the FeNiCrMn HEA exhibits stable and consistent frictional performance regardless of crystallographic orientation.

To further investigate the effects of sliding velocity and friction depth on the tribological behavior of the alloy, the [1$\bar{1}$2] orientation was selected for subsequent simulations based on its optimal performance characteristics: the lowest dislocation line length and relatively lower COF.

3.2 Effect of sliding velocity on tribological performance

To elucidate how sliding velocity influences tribological performance, surface damage evolution is analyzed during abrasive sliding—an indicator critical to evaluating the alloy's tribological response. Fig. 5(a)–(c) illustrates the atomic pile-up morphology at the alloy surface under three different sliding velocities, along with the corresponding maximum atomic pile-up heights and atom loss ratios. Each atom is color-coded based on its relative height from the surface, with red indicating atoms that accumulate on the uppermost surface. Overall, the surface morphologies of the piled-up atoms appear largely consistent across the different sliding velocities. The accumulated atoms are evenly distributed along both sides of the wear track and in front of the abrasive particle, with no observable discontinuities on either side. This suggests that the alloy exhibits good plasticity when sliding along the [1$\bar{1}$2] orientation.

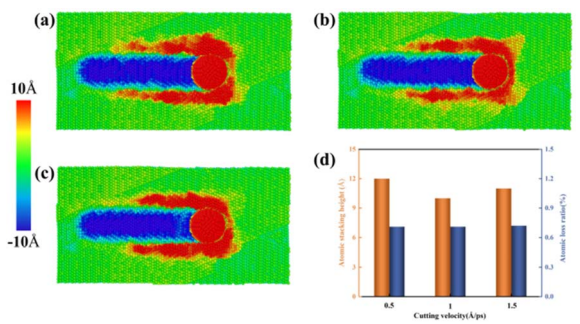

Fig. 5 Surface morphology of the alloy. (a) 0.5 Å ps^{-1}, (b) 1 Å ps^{-1}, (c) 1.5 Å ps^{-1}, (d) maximum atomic pile-up height and atom loss ratio.

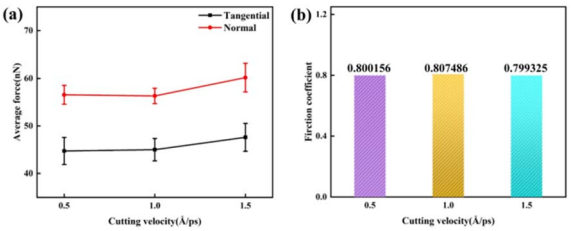

Fig. 6 Average forces and coefficient of friction during the sliding process at different sliding velocities (V). (a) Average tangential and normal forces, (b) coefficient of friction.

To further investigate the effect of sliding velocity on the friction performance, the friction depth (D) was fixed at 15 Å, while three sliding velocities—0.5 Å ps^{-1}, 1 Å ps^{-1}, and 1.5 Å ps^{-1}—were applied to the [1$\bar{1}$2]-oriented alloy model in friction simulations. Fig. 6 displays the average tangential and normal forces exerted on the abrasive particle, as well as the corresponding coefficients of friction under these velocities.

As shown in Fig. 6(a), under a constant friction depth, the variation in sliding velocity exhibits a generally consistent trend in its effect on both tangential and normal forces. At lower velocities, the influence on force is negligible. However, when the velocity increases to 1.5 Å ps^{-1}, both the tangential and normal forces show a noticeable increase. This behavior can be attributed to the following factors: first, high sliding velocities lead to elevated local strain rates. Under such high strain-rate conditions, the material tends to exhibit higher yield strength and enhanced resistance to plastic deformation, thereby requiring greater tangential and normal forces. Second, increasing V results in intensified internal heating of the material, which raises the temperature in the contact region. Although thermal softening makes it easier for the abrasive tool to penetrate the surface, a greater normal force is needed to compensate for the reduction in effective contact area due to softening. Additionally, elevated temperatures may enhance adhesive interactions between surface atoms, requiring increased tangential force to overcome adhesion during sliding. Fig. 6(b) presents the average coefficients of friction under the three sliding velocities. The COFs remain nearly identical across all conditions, indicating that the sliding velocity does not significantly affect the coefficient of friction of the FeNiCrMn HEA.

Fig. 7 presents snapshots of internal damage within the alloy at a sliding distance of 100 Å under three different sliding velocities, along with the corresponding curves of dislocation line length as a function of sliding distance. Overall, the primary form of internal damage during friction is the multiplication and propagation of dislocations. As the abrasive tool moves along the Y-direction, a large number of dislocations are generated beneath the particle. These dislocations are predominantly Shockley partial dislocations with a Burgers vector of 1/6⟨112⟩. As shown in Fig. 7(d), the trend of dislocation line length with increasing sliding distance is consistent across all three sliding velocities. The average dislocation line lengths calculated for each case are also nearly identical. These results

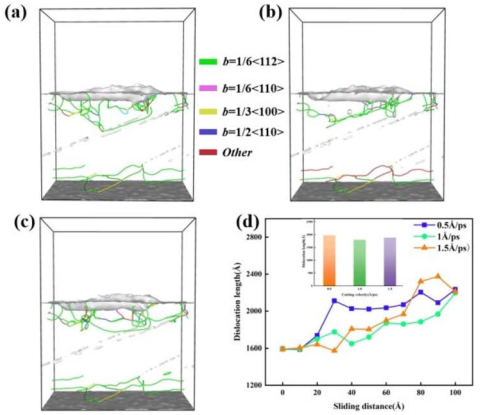

Fig. 7 Dislocation distribution and variation of dislocation line length with sliding distance during steady-state friction of the alloy. (a) 0.5 Å ps^{-1}, (b) 1 Å ps^{-1}, (c) 1.5 Å ps^{-1}, (d) dislocation line length as a function of sliding distance.

indicate that variations in sliding velocity do not significantly affect the extent of internal damage within the alloy during the friction process.

When a material is subjected to friction by an abrasive particle, subsurface damage occurs beneath the wear track. The extent of material damage can be characterized not only by dislocation density but also more intuitively through the atomic stress distribution. In this study, the von Mises criterion[27] was employed to analyze the equivalent stress during the friction process. The equivalent stress is calculated by concentrating the forces acting on all neighboring atoms onto a central atom. Through iterative computation, the atomic-level von Mises stress distribution can be obtained.

Fig. 8 illustrates the atomic stress distributions during the friction process at three different sliding velocities. To facilitate observation of the internal stress variations, a cross-sectional analysis along the *X*-direction was performed for the entire alloy model. Overall, the internal atomic stress distribution is non-uniform, with regions of high-stress atoms present. This non-uniformity is attributed to the high configurational entropy and severe lattice distortion inherent to HEAs.

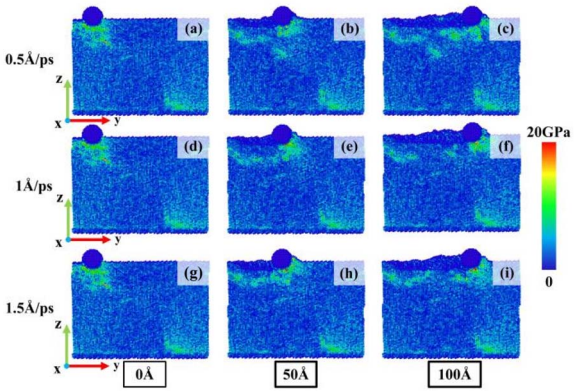

Fig. 8 Atomic stress distribution maps. (a–c) Sliding velocity of 0.5 Å ps^{-1}, (d–f) sliding velocity of 1 Å ps^{-1}, (g–i) sliding velocity of 1.5 Å ps^{-1}.

As the abrasive tool begins to indent and penetrate the alloy, stress concentration emerges beneath the particle. This phenomenon arises due to the disruption of the original lattice structure, which causes atoms to be displaced from their lattice sites to higher-energy positions, as shown in Fig. 8(a), (d) and (g). With increasing sliding distance, high-stress atoms are observed not only beneath the abrasive tool but also beneath the wear track. Notably, as the sliding velocity increases, the number of high-stress atoms beneath the wear track decreases and their distribution becomes more continuous. This indicates that higher sliding velocities result in reduced frictional fluctuations and a more stable sliding process. A comparison between Fig. 7 and 8 reveals that regions containing high-stress atoms consistently coincide with the presence of dislocations. This suggests that the accumulation and entanglement of dislocations contribute to localized stress concentration. In contrast, high-stress atoms observed in the central region of the alloy are primarily attributed to dislocation slip, which serves to release the internal stress accumulated within the material.[28]

3.3 Effect of friction depth on tribological performance

To investigate the influence of friction depth on the tribological performance of the alloy and to elucidate the underlying mechanisms of the wear process, the sliding velocity was fixed at 1 Å ps^{-1}, while friction depths of 10 Å, 15 Å, and 20 Å were applied. Fig. 9 presents the surface morphology of the alloy after the abrasive tool traveled a sliding distance of 100 Å. It was observed that at a friction depth of 10 Å, the worn atoms were primarily distributed on both sides of the wear track, with minimal atomic accumulation at the front of the abrasive particle. As the friction depth increased, atoms began to accumulate at the particle's leading edge. This can be attributed to the initial indentation stage, where worn atoms are mainly displaced around the abrasive. When sliding commences, deeper indentation results in a larger contact area between the abrasive tool and the alloy, enhancing the adhesive interactions. Consequently, the worn atoms are more likely to adhere to the front of the abrasive tool and less likely to be displaced to the sides of the wear track. As sliding progresses, this adhesion leads to the formation of a pile-up of atoms at the abrasive front. Both the maximum atomic pile-up height and the atom loss ratio increase with increasing friction depth. This trend can be

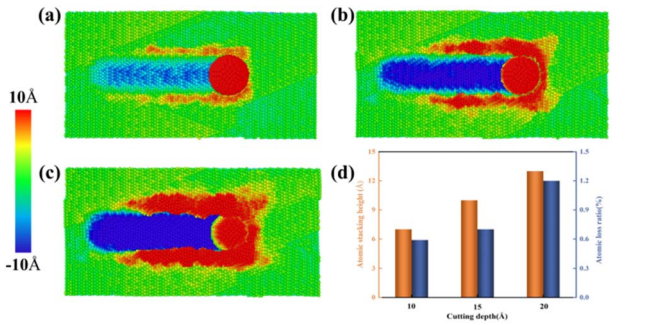

Fig. 9 Surface morphology of the alloy. (a) 10 Å, (b) 15 Å, (c) 20 Å, (d) maximum atomic pile-up height and atom loss ratio.

explained by two primary factors: (1) a greater friction depth results in a larger volume of material being penetrated by the abrasive, thereby disrupting more atomic planes over the same sliding distance. This causes a larger number of atoms to be displaced from the alloy lattice, forming surface pile-ups as worn atoms. (2) With increased indentation depth, the contact area between the abrasive tool and the alloy expands, allowing more worn atoms to adhere to the particle surface. These adhered atoms, in turn, contribute to further wear of the alloy as they move in conjunction with the abrasive.

Fig. 10 summarizes the average tangential force, average normal force, and coefficient of friction under different friction depths during the sliding process. It can be observed that as the indentation depth increases, both the average forces and the coefficient of friction exhibit an increasing trend. Additionally, the error bars associated with the tangential and normal forces also become larger, indicating greater fluctuations in force measurements. With increasing penetration depth, the projected contact area between the abrasive tool and the alloy significantly enlarges, resulting in higher normal stresses. Meanwhile, the true contact area governs the magnitude of the tangential force; as the abrasive penetrates deeper, the atomic-scale contact area increases, leading to greater tangential forces. The coefficient of friction, defined as the ratio of tangential force to normal force, also increases accordingly. As shown in Fig. 10(a), the tangential force increases at a faster rate than the normal force, which directly contributes to the rising trend in the coefficient of friction.

Fig. 11 presents the evolution of dislocations within the alloy during the abrasive wear process. Overall, it is evident that with increasing friction depth, the total dislocation line length increases. Additionally, dislocation length gradually rises as the sliding distance increases. This trend is primarily attributed to the increase in the number of atomic planes contacted and disrupted by the abrasive tool during deeper penetration, resulting in more extensive lattice destruction and, consequently, greater dislocation generation. Notably, as the indentation depth increases, the number of dislocations propagating into the interior of the alloy also increases, indicating more severe subsurface damage. At a friction depth of 20 Å, the presence of stair-rod dislocations with a Burgers vector of $b = 1/6\langle 110\rangle$ is observed, which is absent at the lower friction depth of 10 Å, as shown in Fig. 11(a). Previous studies have shown that stair-rod dislocations are immobile dislocations formed by the

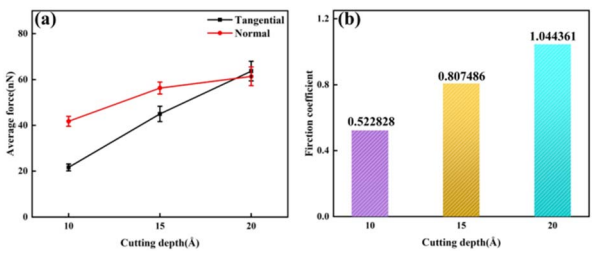

Fig. 10 Average forces and coefficient of friction during the sliding process at different friction depths (*D*). (a) Average tangential and normal forces, (b) coefficient of friction.

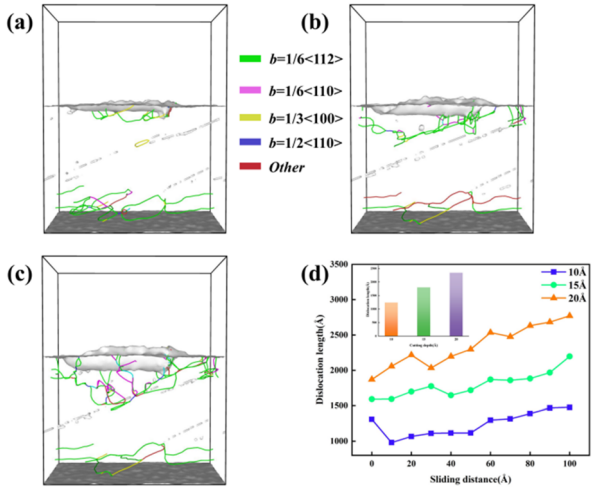

Fig. 11 Dislocation distribution and variation of dislocation line length with sliding distance during steady-state friction of the alloy. (a) 10 Å, (b) 15 Å, (c) 20 Å, (d) dislocation line length as a function of sliding distance.

reaction of two Shockley partial dislocations. When two $1/6\langle 112\rangle$ Shockley partials glide on intersecting slip planes, a stacking fault is created, and their intersection forms a stair-rod dislocation. These immobile dislocations contribute to local strain hardening,[29] which is one of the factors responsible for the increased tangential and normal forces observed at greater indentation depths. Despite the emergence of stair-rod dislocations at higher depths, the dominant dislocation type remains the Shockley partial dislocation with $b = 1/6\langle 112\rangle$. Their presence serves as a mechanism to relieve local stresses induced by the abrasive tool during sliding—an inherent characteristic of this HEA.

Fig. 12 presents the atomic stress distributions within the alloy during the friction process. From Fig. 12(a), (d) and (g), it can be observed that internal stress accumulation increases with greater friction depth. This is primarily due to the increased number of disrupted atomic planes as the indentation depth grows, causing atoms to deviate from their original

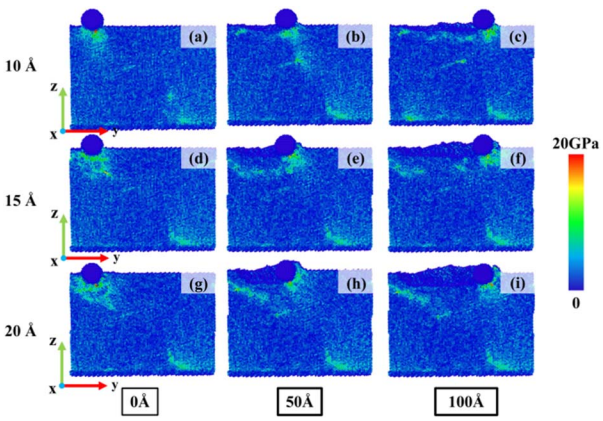

Fig. 12 Atomic stress distribution maps. (a–c) Friction depth of 10 Å, (d–f) friction depth of 15 Å, (g–i) friction depth of 20 Å.

equilibrium lattice positions and resulting in localized stress concentration. Furthermore, the destruction of lattice planes tends to create vacancies, which serve as primary nucleation sites for dislocations. When vacancies cluster together, they create localized distortion zones in the lattice, which significantly reduce the critical energy required for dislocation loop formation. At the same time, vacancy clusters induce shear strain through local lattice contraction, causing adjacent atomic planes to slip relative to one another and thereby directly generating dislocation loops. The local accumulation and entanglement of dislocations further intensify the atomic stress levels. As the abrasive tool continues to slide, dislocations glide along their respective slip planes, facilitating the release of stress. However, this stress is subsequently transmitted deeper into the alloy. Fig. 12(b), (e) and (h) reveal that deeper indentation depths lead to the formation of stair-rod dislocations, which are immobile and incapable of relieving stress. Consequently, high-stress atoms persist beneath the wear track. In contrast, no stair-rod dislocations are observed in the alloy with a friction depth of 10 Å, and the stresses generated during sliding are effectively relieved *via* the movement of Shockley partial dislocations. At a sliding distance of 100 Å, only a limited number of high-stress atoms remain beneath the wear track. This is mainly because the accumulated stresses have been transmitted by the abrasive tool to both sides of the wear track. This phenomenon is clearly illustrated in Fig. 9, where an increase in indentation depth corresponds to a greater accumulation of atoms along both sides of the wear track.

One of the ultimate goals of molecular dynamics simulations is to guide the development and optimization of new materials while reducing the cost of "trial and error." This study provides deep insights into the friction and wear behavior of FeNiCrMn HEAs, highlighting their great potential as high-performance wear-resistant coatings or surface modification materials—for example, in applications such as aircraft engine blades, precision bearings, and artificial joints, where exceptional wear resistance is required. Our simulations enable the evaluation of tribological responses at the atomic scale under varying friction depths and sliding velocities. Although the simulation conditions are extreme, the revealed mechanisms can be extrapolated to inform the selection of suitable operating parameters in macroscopic experiments, thereby avoiding direct testing under high-risk and high-cost conditions. At the same time, we encourage future experimental studies—for instance, detailed analyses of subsurface wear structures using transmission electron microscopy (TEM)—to validate these atomic-scale structural evolutions. Our simulations provide clear targets and directions for such experimental verification.

4. Conclusion

The friction and wear behavior of FeNiCrMn HEA was investigated using MD simulations. The study systematically examined the effects of different crystallographic orientations, sliding velocities, and friction depths on surface and subsurface damage, worn atom distribution, dislocation evolution, as well as the tangential force, normal force, and coefficient of friction during the sliding process. The aim was to provide theoretical insights that may support the future development and application of FeNiCrMn HEA. The main conclusions are as follows:

(1) Under different crystallographic orientations, the coefficient of friction of the FeNiCrMn HEA remains largely consistent. However, the distribution of worn atoms and dislocations during the friction process varies significantly. This is attributed to the fact that different crystallographic orientations activate different slip systems for dislocation motion. Among the orientations studied, the $[1\bar{1}2]$ orientation exhibits a shorter dislocation line length and a relatively lower coefficient of friction.

(2) The sliding velocity has minimal effect on the coefficient of friction, dislocation line length, and atomic stress distribution of the FeNiCrMn HEA during the friction process. However, as the velocity increases to 1.5 Å ps^{-1}, both the tangential and normal forces acting on the abrasive tool exhibit an upward trend. High-speed sliding leads to an increase in the local strain rate, and under such high strain-rate conditions, the material demonstrates higher yield strength and enhanced resistance to deformation. Simultaneously, internal heating intensifies, contributing to the increase in both tangential and normal forces.

(3) Variations in friction depth have a significant impact on the overall friction and wear performance of the alloy. As the indentation depth increases, a greater number of atomic planes are disrupted by the abrasive particle. For the same sliding distance, higher tangential and normal forces are required to break more atomic bonds. The more atoms that are displaced, the greater the number of worn atoms and defects generated. These defects serve as nucleation sites for dislocations. The accumulation and entanglement of dislocations lead to localized atomic stress concentration, while the slip of dislocations facilitates the release of these stresses.

Author contributions

All authors participated in the discussion and interpretation of the results. All authors edited and proofread the final manuscript.

Conflicts of interest

There are no conflicts to declare.

Data availability

The data that support the findings of this study are available within the article.

Acknowledgements

This work was financially supported by the Gansu Provincial Natural Science Foundation (25JRRM005, 25JRRM004, and 24JRRA738).

References

1 J. W. Yeh, S. K. Chen, S. J. Lin, J. Y. Gan, T. S. Chin, T. T. Shun, C. H. Tsau and S. Y. Chang, *Adv. Eng. Mater.*, 2004, **6**, 299–303.
2 W. L. Hsu, C. W. Tsai, A. C. Yeh and J. W. Yeh, *Nat. Rev. Chem.*, 2024, **8**, 471–485.
3 M. Luebbe, J. Duan, F. Zhang, J. Poplawsky, H. Pommeranke, M. Arivu, A. Hoffman, M. Buchely and H. Wen, *Mater. Sci. Eng., A*, 2023, **870**, 144848.
4 R. Song, L. Wei, C. Yang and S. Wu, *J. Alloys Compd.*, 2018, **744**, 552–560.
5 Y. Geng, W. Chen, H. Tan, J. Cheng, S. Zhu, J. Yang and W. Liu, *Research*, 2023, **6**, 0160.
6 W. Zhai, L. Bai, R. Zhou, X. Fan, G. Kang, Y. Liu and K. Zhou, *Adv. Sci.*, 2021, **8**, 2003739.
7 W. Chen, N. Li, F. Wang, J. Gu, J. He and M. Song, *J. Alloys Compd.*, 2022, **918**, 165651.
8 J. Li, Q. Fang, *et al.*, *RSC Adv.*, 2016, **6**(80), 76409–76419.
9 Y. Zhang, W. Yang, J. Peng, *et al.*, *RSC Adv.*, 2024, **14**(26), 18258–18270.
10 M. Zhang, Z. Jiang, M. Niu, Y. Sun and X. Zhang, *Wear*, 2022, **508–509**, 204471.
11 Z. Guo, A. Zhang, J. Han and J. Meng, *Tribol. Int.*, 2020, **151**, 106436.
12 Z. Zhang, H. Li, C. Si, S. Xu and J. Wang, *Wear*, 2025, 206205.
13 Y. Ruan, C. Yin, X. Liu, D. Zhang, J. Wu and Z. Zhu, *J. Alloys Compd.*, 2025, **1024**, 180183.
14 Z. Gan, Y. Huang, C. Wu, T. Yang, S. Shen, G. Luo and J. Liu, *Mater. Sci. Eng., A*, 2024, **895**, 146213.
15 R. Yang, X. Guo, H. Yang and J. Qiao, *Surf. Coat. Technol.*, 2023, **464**, 129572.
16 Y. Lu, M. Zhang, L. Zhang, P. Yu, R. Li, X. Liu, Y. Zhang and G. Li, *Mater. Sci. Eng., A*, 2021, **801**, 140421.
17 R. Yang, F. Li, Z. Huang, Y. Li and H. Yang, *Tribol. Int.*, 2024, **200**, 110084.
18 A. Zhou, X. B. Liu, Q. Wang, S. Y. Zhang, Y. Meng, H. B. Zhou and S. H. Zhang, *Tribol. Int.*, 2023, **180**, 108258.
19 G. Li, T. Yu, P. Wu and M. Chen, *Wear*, 2023, **522**, 204849.
20 A. P. Thompson, H. M. Aktulga, R. Berger, D. S. Bolintineanu, W. M. Brown, P. S. Crozier, P. J. in 't Veld, A. Kohlmeyer, S. G. Moore, T. D. Nguyen, R. Shan, M. J. Stevens, J. Tranchida, C. Trott and S. J. Plimpton, *Comput. Phys. Commun.*, 2022, **271**, 108171.
21 M. S. Daw and M. I. Baskes, *Phys. Rev. B:Condens. Matter Mater. Phys.*, 1984, **29**, 6443.
22 A. Daramola, G. Bonny, G. Adjanor, C. Domain, G. Monnet and A. Fraczkiewicz, *Comput. Mater. Sci.*, 2022, **203**, 111165.
23 J. Tersoff, *Phys. Rev. Lett.*, 1988, **61**, 2879.
24 A. Stukowski, *Modell. Simul. Mater. Sci. Eng.*, 2010, **18**, 015012.
25 J. Ren, Y. Ge, W. Li, Q. Gao, Q. Wang, J. Li, H. Xue and X. Lu, *J. Mater. Sci.*, 2025, **60**, 5442–5458.
26 T. Dyck, P. Ober-Wörder and A. Bund, *Wear*, 2016, **368–369**, 390.
27 H. Xie, Z. Ma, H. Zhao and L. Ren, *Mater. Today Commun.*, 2022, **30**, 103072.
28 A. Kedharnath, R. Kapoor and A. Sarkar, *Comput. Struct.*, 2021, **254**, 106807.
29 Z. Hao, Z. Li and Y. Fu, *Arch. Civ. Mech. Eng.*, 2024, **24**, 39.